Polymorphism of gold under laser-based ramp compression to 690 GPa

Sirus K. Han [1,*] Raymond F. Smith,[2] Donghoon Kim [1] June K. Wicks,[1,†] J. Ryan Rygg,[3] Amy Lazicki,[2]
Jon H. Eggert [2] and Thomas S. Duffy[1]

[1]*Department of Geosciences, Princeton University, Princeton, New Jersey 08544, USA*
[2]*Lawrence Livermore National Laboratory, Livermore, California 94550, USA*
[3]*Laboratory for Laser Energetics, University of Rochester, Rochester, New York 14623, USA*

The high-pressure behavior and polymorphism of gold have attracted strong recent interest from theory as well as from both static and dynamic experiments. In this study, gold was dynamically ramp-compressed to 690 GPa via laser ablation using the Omega Laser Facility (University of Rochester) in order to investigate the stability regions of this noble metal's polymorphs. Stresses were determined from measurements of surface or interface velocities by laser interferometry. *In situ* x-ray diffraction was carried out to constrain the structure and density. The ambient face-centered-cubic (fcc) phase was observed at 162 GPa, followed by a mixed-phase region consisting of the fcc and body-centered-cubic (bcc) phases. The presence of only the bcc phase was observed between 377 and 690 GPa. Our results are consistent with recent shock-compression experiments and demonstrate that gold transforms to the bcc phase under conditions of both ramp and shock loading.

I. INTRODUCTION

Gold is a $5d$ transition metal with a complex electronic structure that has been the subject of extensive study at high-pressure–high-temperature conditions [1–11]. Due to its chemical inertness, low strength, moderate compressibility, simple diffraction pattern, wide phase stability, and commercial availability, gold is widely used as an *in situ* standard for static high-pressure experiments [1]. Consequently, there is an extensive literature of experimental and theoretical determinations of its equation of state [1–5,12–18]. Gold is also a standard material for studies under conditions of warm dense matter [19–21] and the development of static ultrahigh-pressure experimental techniques [22–24].

While gold is known to persist in its ambient face-centered-cubic (fcc) structure over a wide range of pressures and temperatures [23,24], recent theoretical studies have predicted that gold will undergo phase transitions at extreme conditions. There is, however, disagreement regarding the stable phase(s) and transition pressures [5–9,25,26]. At low temperatures (0–300 K), several calculations predict a transition from the fcc phase to the hexagonal-close-packed (hcp) phase with a predicted transition pressure ranging from 151 to 410 GPa [5,7,8]. Other studies predict a transition from the fcc phase to a double-hexagonal-close-packed (dhcp) phase at 232–250 GPa [9,25], or that gold transforms to a series of stacking disordered phases above 390 GPa [26]. A phase transition sequence from fcc to hcp to a body-centered-cubic (bcc) phase has also been predicted with the latter transformation occurring at 400–520 GPa [6,8]. Only a few theoretical studies have

extended the examination of gold to higher temperatures. At ∼1000 K, one calculation found that the fcc phase transforms directly to the hcp phase at 670 GPa [26], whereas another calculation reported that the pressure stability field of the hcp phase contracts with increasing temperature and that the fcc phase transforms directly to the bcc phase at ∼380 GPa and 2000 K [6].

Experimental tests of these predictions have been limited by the difficulty of performing structural measurements at the requisite pressures and temperatures. Transformation to the hcp phase was reported in an x-ray diffraction experiment at 248 GPa and 860 K using an electrically heated diamond anvil cell (DAC) [9]. The fcc-hcp transition was observed to have a positive Clapeyron slope, and the hcp phase was retained on quenching to room temperature [9]. In other experiments using newly developed anvil designs, only the fcc phase was observed up to 1.065 TPa under room-temperature compression [23,24].

In shock-compression experiments on gold using plate impact techniques, no evidence of a phase transition was observed along the Hugoniot to 550 GPa [3]. However, only the density was determined in these experiments via measurement of shock and particle velocities, and no direct, atomic-level structural information was obtained. Because of this, phase transitions with small density changes may not be detected in such experiments. More recently, shock experiments using nanosecond laser compression techniques combined with synchrotron x-ray diffraction have reported conclusive evidence for a transition to the bcc phase followed by melting along the Hugoniot, underscoring the importance of *in situ* x-ray measurements [10,11]. In these experiments, the bcc phase was first observed as part of a mixed-phase assemblage with the fcc phase at 176 GPa. The completely transformed bcc phase was then observed as part of a mixed phase with liquid at 220 GPa and persisted until complete melting was observed at

─────────
*sirush@princeton.edu
†Present address: Department of Earth and Planetary Sciences, Johns Hopkins University, Baltimore, Maryland 21218, USA.

350 GPa (pressures from Ref. [11] and results from Ref. [10] are qualitatively consistent, but phase boundaries are shifted by +47, +42, and −28 GPa, respectively). In a related study, the presence of abundant stacking faults was determined based on x-ray diffraction line shifts of laser-compressed gold at 50–150 GPa [27]. These stacking faults may be important in promoting structural transformations in shocked noble metals [28].

Ramp compression is an alternative dynamic loading technique that provides access to lower-temperature compression pathways than shock compression [29]. Laser-based ramp compression combined with pulsed x-ray diffraction can provide constraints on equations of state and phase transitions into the terapascal regime [30–33]. In this study, we use the Omega laser to ramp-compress gold to nearly 700 GPa in order to constrain its phase behavior into the multimegabar regime.

II. METHODOLOGY

A. Experimental geometry

The gold samples used in these experiments were 2.5- or 3-μm-thick rolled foils obtained from Goodfellow (99.9% purity). Target assemblages were created by sandwiching the foils between a diamond ablator and an optical window (diamond or LiF; see Table S1 of the Supplemental Material [34]). Higher-pressure shots also included a thin ($\sim$1 μm thick) layer of gold as a heat shield within the ablator to attenuate x rays emitted from the ablation plume. The heat shield melts as a result of x-ray irradiation during compression, and no crystalline diffraction is recorded from it. These target assemblages were affixed to a Ta (100 μm thick), W (100 μm thick), or Pt (75 μm thick) plate with a 300-μm-diameter pinhole aligned to the target's center [Figs. 1(a) and 1(b)]. Glue layers were 1 ± 0.2 μm thick [35]. The target package was mounted onto an image-plate-lined box, as shown in Fig. 1(c) [35,36]. An aperture in the back of the box (directly opposite the target package) allowed for optical access for Doppler velocimetry measurements [37].

Experiments were carried out at the Omega-EP and the Omega-60 lasers at the Laboratory for Laser Energetics at the University of Rochester. Omega-EP consists of four independent UV (351 nm) lasers, which can each produce shaped pulses of 1–10 ns duration and were used to deliver up to 1.5 kJ per beam [38]. The Omega-60 laser is a 30-kJ laser (500 J/beam) that consists of 60 individual 351-nm beams, each of which can be individually shaped and timed [39]. Our experimental procedure follows earlier studies performed using these facilities [30–32,40].

Samples were compressed by laser ablation. Individual or composite laser pulses were focused on the front surface of the diamond ablator. For sufficient laser irradiance, this generates a rapidly expanding plasma, which, by conservation of momentum, drives a uniaxial pressure wave into the target package. An empirical scaling law between applied intensity and stress achieved is given as [41]

$$\sigma(t) \, (\mathrm{GPa}) = 42 \times [I(t) \, (\mathrm{TW/cm^2})]^{0.71}, \qquad (1)$$

where $\sigma(t)$ is the stress history and $I(t)$ is the laser intensity history. By varying the intensity and shape of the composite
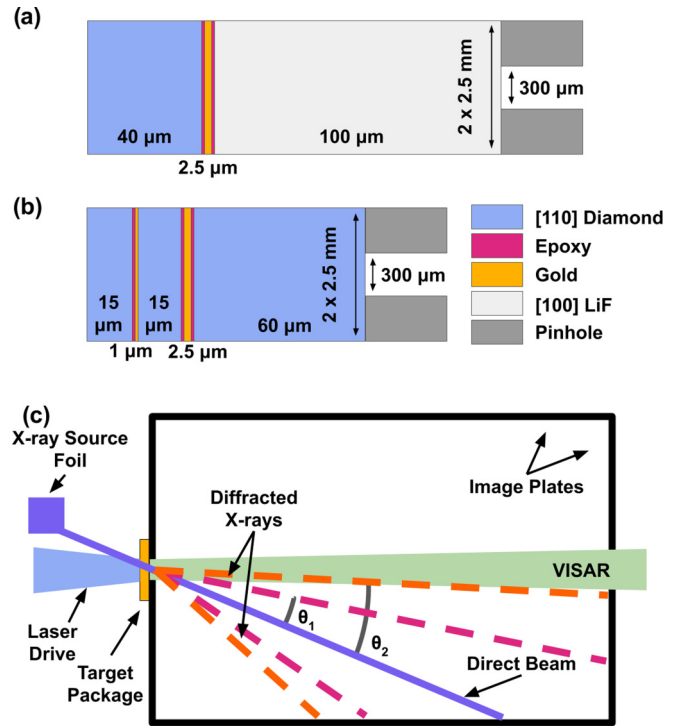

FIG. 1. (a) and (b) Target packages used in this study (not to scale). "Pinhole" refers to the high-Z material (Ta, W, or Pt) containing a 300-μm-diameter aperture (Table S1 of the Supplemental Material). The target configuration shown in (a) was used in lower-stress shots, while the configuration shown in (b) was used in higher-stress experiments. (c) Schematic of experimental geometry for these experiments. Target packages in (a) and (b) were affixed to the front of the target box, in the position marked in yellow. Colored dashed lines show a two-dimensional cross section of representative diffraction cones.

drive pulse, longitudinal stress states between 162(12) and 690(56) GPa were obtained in this study.

At Omega-EP, compression was driven by a single 10-ns-duration laser pulse, which was focused to a 1.1-mm-diameter spot on the surface of the diamond ablator. At Omega-60, compression was driven by four to six 1–3.5-ns-duration 351-nm laser pulses which were focused to an 0.8-mm-diameter spot. These individual pulses were timed to form a composite pulse with a ramp profile [Fig. 2(a)]. Focal-spot intensities were spatially smoothed using distributed phase plates which were also used to define the focal spot with a super-Gaussian profile. Pulse shapes from both Omega-60 and Omega-EP are shown in the Supplemental Material [34]. In each experiment, the sample was first compressed by an elastic shock arising from the diamond ablator [42], which shock-compressed the sample to $\sim$70 GPa. This was followed by a weak release and then ramp compression to the final stress [see Fig. 2(b)].

B. Stress determination

Interface or free surface velocities were recorded using a line-imaging velocity interferometry system for any reflector (VISAR) [37]. A 532-nm laser was focused on the back surface of the target package, reflecting from either the diamond free surface (higher-stress shots) or the sample-LiF interface
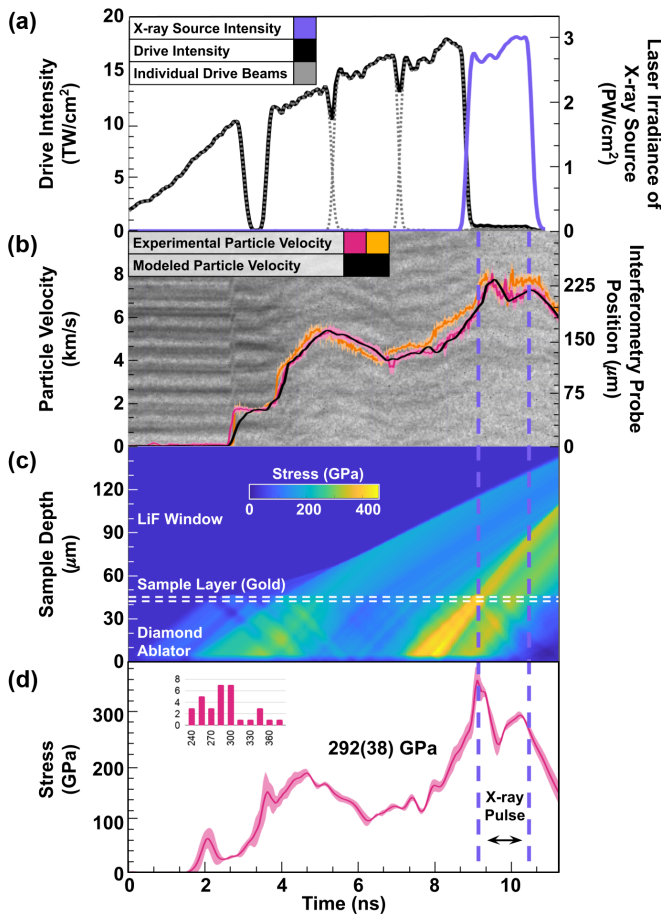
FIG. 2. Laser pulses, interferometry, and stress determination via hydrocode simulations. (a) Composite laser pulse for a representative experiment, shot 85590, at Omega-60. (b) Measured Au and LiF particle velocity histories (magenta and orange, respectively) recovered from interferometry data (grayscale). Pressure drives are iteratively forward modeled using the HYADES hydrocode [43], until the calculated particle velocity history (black) converges on the experimental data. (c) Longitudinal stress as a function of position within the target assemblage and time associated with the modeled velocity history in (b). The white dashed lines mark the sample layer, while purple dashed lines mark the duration of the x-ray pulse. (d) Longitudinal stress history averaged over the gold layer (line), with standard deviation across the depth of the gold layer (shaded). The inset is a histogram of sampled stress states in gold separated into 50-ps bins.

(lower-stress shots) as seen in Fig. 1(c). Light reflected from the sample was directed through an interferometer which produces phase shifts proportional to surface or interface velocity. Phase as a function of time was extracted from VISAR images using a fast Fourier transform algorithm and then converted to velocities. Due to the 2π limitation of a fringe shift measurement, two channels with different sensitivities were used in order to unambiguously resolve any velocity changes that occur when the fringe frequency exceeds the system response, with typical fringe sensitivities between 3 and 20 km/s per fringe. The data were recorded using a streak camera with a temporal resolution of 20 ps [37]. An example velocity profile is shown in Fig. 2(b).

Stress histories were obtained from measured velocity histories in one of two ways. For shots using a LiF window, a stress history was derived from the sample-window interface-velocity history using HYADES [43], a hydrodynamics code package. HYADES uses equation-of-state information and an estimated pressure drive to simulate dynamic compression by solving the equations of mass and energy transport. An initial estimate for the applied stress drive was obtained using Eq. (1). Next, a series of HYADES forward models were constructed, iterating over the applied pressure drive, until the modeled velocity history converged upon experimental velocity histories, as seen in Fig. 2(b). The peak and width of the resultant sample pressure distribution were then associated with the centroid d spacing of the x-ray diffraction peaks {Figs. 2(c) and 2(d) and the Supplemental Material [34]; see Refs. [35,36] for further details}. Note that a symmetrical distribution of pressure states around a mean value will result in a broadening of the diffraction peaks but will not alter the measured centroid d spacing. Variations in stress in these experiments are due to the large impedance mismatch between gold and diamond, requiring additional reverberations to homogenize stress within the sample.

For higher-stress shots using a diamond window, the ramp equation of state of diamond [42] was used to integrate backwards from the free surface of the window to the sample layer using the method of characteristics [44]. The resultant map of stress as a function of time and position was averaged over the temporal duration of the x-ray pulse and over the spatial range of the sample layer [34].

Stress uncertainty was calculated by considering four contributions: (i) uncertainty in the equation of state of the window material (this is estimated as ±3% of the total stress and is systematic); (ii) spatial and temporal heterogeneity of stress over the sample thickness and the duration of the x-ray pulse (this is estimated as the standard deviation across the sampled time and thickness and is dominated by temporal variation, as the reverberation of compression waves within the gold layer rapidly brings the material to a uniform stress state); (iii) uncertainty in measured velocities due to limited etalon sensitivity (the accuracy with which a fringe shift can be measured is ~3% and, coupled to the velocity per fringe, gives a measure of velocity uncertainty); (iv) uncertainty in reported target package layer thicknesses, which is estimated as ±0.05% of the total stress. Uncertainties (ii)–(iv) are random and uncorrelated and are added in quadrature to uncertainty (i), which is systematic but uncorrelated to the other sources of uncertainty.

A final factor in determining stress is the strength behavior of the diamond window. If diamond loses strength on unloading, then stress is systematically underestimated, as modeled stress would lie along the lower-stress unloading path. This systematic underestimation is taken as +50 GPa over the stress range of this study as described in Ref. [33] and applies only to the three highest-stress shots which used diamond windows.

C. X-ray diffraction

X-rays were generated by laser-irradiation-induced ionization of a copper foil, creating heliumlike nuclei which
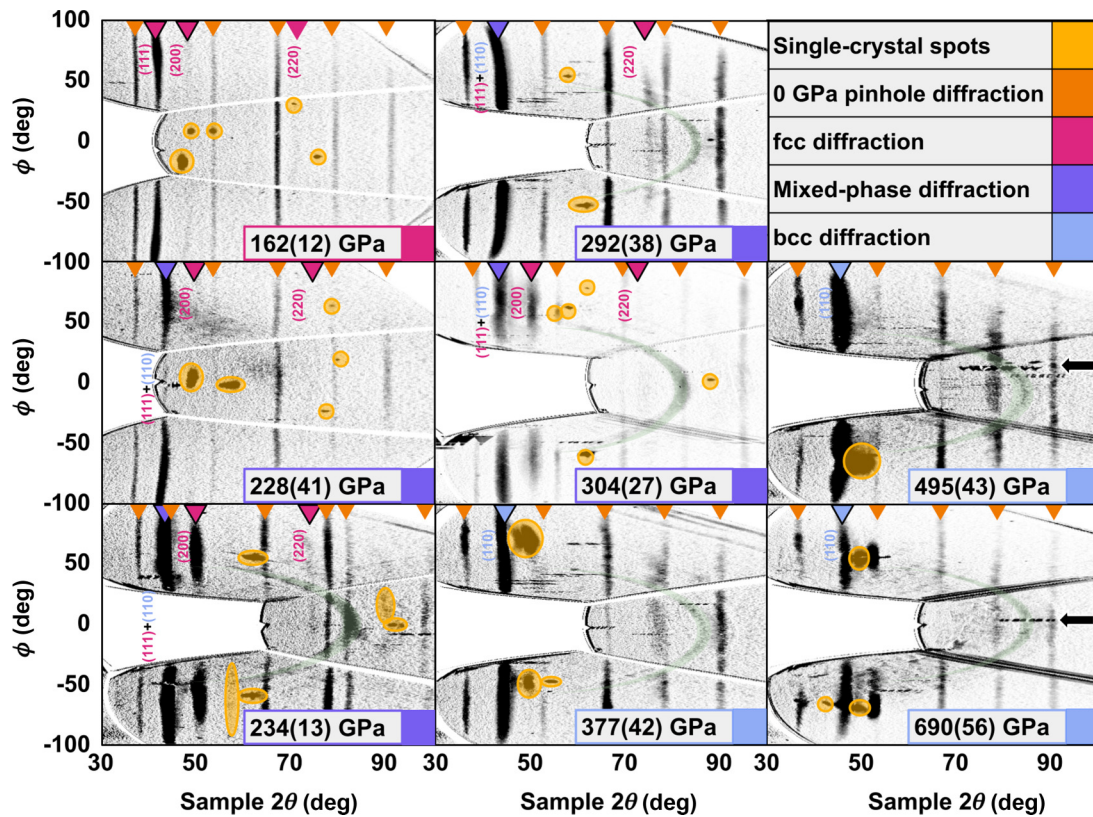
FIG. 3. X-ray diffraction data for gold. ϕ refers to the azimuthal angle around the diffraction cone, 2θ is the diffraction angle (wavelength is fixed at 1.482 Å). Smaller orange triangles denote diffraction lines from the ambient-pressure pinhole material. Larger magenta, purple, and blue triangles denote sample peaks from assignment to an fcc, mixed, or bcc phase, respectively. Sharp spots are highlighted in yellow and represent Laue diffraction from single-crystal LiF and diamond arising from spectrally broad thermal emission emanating from the x-ray source plasma. Sharp horizontal bars at $\phi \sim 0°$ and indicated in the rightmost panels by black arrows are artifacts of the image filtration used. Curved features (apex at $\phi = 0°$, $2\theta \sim 85°$, marked in green) above 234(13) GPa are diffraction from components of the experimental box. See the Supplemental Material [34] for this and for integrated lineouts.

emitted quasimonochromatic He$_\alpha$ x-rays of wavelength 1.482(2) Å [45]. At Omega-EP, the foil was positioned 24 mm from the target at an angle of 21.5° from the target normal. It was irradiated by a single beam with a 1-ns flat-top pulse shape focused to a 200-μm spot with a peak intensity of $\sim$3 PW/cm^2. Pulses of this intensity generate $\sim$10^{11} photons at the position of a 300-μm-diameter pinhole [45]. At Omega-60, the foil was placed 45° from the target normal and 24 mm from the target and was irradiated by 26 beams, each with a 1-ns flat-top pulse shape, temporally coincident and focused to a 300-μm spot, reaching total peak intensities of $\sim$2–4 PW/cm^2, divided across both surfaces of the copper foil.

The generated x-rays passed through the compressed target package, diffracted from the sample, were collimated by the pinhole, and were recorded on image plates lining the sides of the steel target box. The image plates were lined with 12.5-μm-thick Cu foils which filtered out higher-energy satellite lines of the He-like emission spectrum [36,45]. Visible light was blocked using a 25-μm-thick layer of black Kapton. The image plates were shielded from secondary emission from the incidence of the direct x-ray beam by a tantalum cone affixed to the bottom image plate in the target box.

The x-ray diffraction data were transformed from Cartesian coordinates to $(2\theta, \phi)$ space, where 2θ is the diffraction angle

and ϕ refers to the azimuthal angle around the diffraction cone [34]. This transformation used diffraction lines from the uncompressed pinhole material as a reference to constrain the 11 geometric degrees of freedom of the target box (two angular for the x-ray source, three translational for the pinhole location, one translational for each of the side image plates, and two translational for the back image plate) [36]. An illustration of this transformation is shown in the Supplemental Material [34]. A sensitive nonlinear iterative peaks (SNIP) background subtraction was then applied to each of the transformed image plates in order to estimate and subtract the background [35]. All of the transformed and filtered image plates are shown in Fig. 3, while integrations of the main sample peaks are shown in the Supplemental Material [34].

At high absolute values of ϕ, sample peaks curve towards lower values of 2θ. This can be seen in, for example, the panel at 292(38) GPa in Fig. 3. This curvature arises from the finite lateral extent of the laser drive. This introduces edge effects, in which sample material farther from the lateral center of the package is less compressed. High absolute values of ϕ selectively sample diffraction from these lateral areas. This effect can be seen in other laser-driven ramp-compression experiments of metals using similar geometries, e.g., Refs. [46,47]. To avoid the effects of edge unloading, line profiles were

generated by restricting the integration to either $\pm 50°$ or $\pm 75°$ in ϕ and fit using a constant background and Gaussian peak profiles.

Systematic corrections were applied to each of the pinhole peak positions to account for the finite displacement of both the sample and the pinhole substrate from the pinhole center. These corrections are described in detail in Ref. [35]. The average correction applied in this way was approximately $-0.13°$ with a maximum correction magnitude of $0.33°$. Another correction was then applied to each of the sample peak positions to account for inconsistencies in the dewarping routine by comparing the measured positions of the uncompressed pinhole material peaks to known values for the pinhole material. This correction was calculated as

$$\Delta d_0 = \frac{(d_0 - \mathrm{PH}_2)}{l_{1-2}}\Delta \mathrm{PH}_1 + \frac{(d_0 - \mathrm{PH}_1)}{l_{1-2}}\Delta \mathrm{PH}_2, \quad (2)$$

where Δd_0 is the correction applied to the peak position d_0, PH_1 is the measured position of the pinhole peak directly to the left of the sample peak, PH_2 is the measured position of the pinhole peak directly to its right on the image plate, $\Delta \mathrm{PH}$ is the deviation between a given pinhole peak's measured position and its known ambient position, and l_{1-2} is the distance between the measured pinhole peak locations. The average correction applied in this way was $-0.11°$ with a maximum correction magnitude of $0.24°$.

Sources of uncertainty considered for determination of the d spacing were the uncertainty in the incident x-ray wavelength (10 eV, <0.01 Å [45]), the resolution of the image plates (typically ~ 0.01 Å [35,36]), and the uncertainty in peak fitting (<0.01 Å). The timing of the x-ray pulse was taken to begin when the composite x-ray source laser pulse reached 80% of its maximum intensity and taken to end when it fell to 80% at the end of the pulse. An additional 0.1 ns was added to account for the propagation time from the x-ray source to the target.

Lattice parameters and corresponding densities of the fcc phase were calculated at all stresses using only the highest-intensity (111) reflection for consistency. The (200) peak position is known to be sensitive to stacking faults and nonhydrostatic stress [27,48], while the (220) peak intensity was low.

III. RESULTS

Eight shots, which spanned a stress range of 162(12) to 690(56) GPa, were performed. Figure 3 shows the set of x-ray diffraction patterns generated in this study. The associated d spacings are plotted as a function of stress in Fig. 4 alongside calculated diffraction patterns for three candidate phases of gold: fcc ($Fm\bar{3}m$, $Z = 4$), hcp ($P6_3/mmc$, $Z = 2$), and bcc ($Im\bar{3}m$, $Z = 2$) (see also Table S2 in the Supplemental Material). Expected d spacings for candidate phases were obtained from unit cell volumes using a third-order Birch-Murnaghan equation of state for each phase. A bulk modulus K_0 of 167 GPa and first derivative of the bulk modulus K_0' of 5.71 were used for the fcc phase [2] and assumed for the hcp and bcc phases, for which equation-of-state information is unavailable. An ideal c/a ($=1.633$) ratio was assumed for the hexagonal phase.
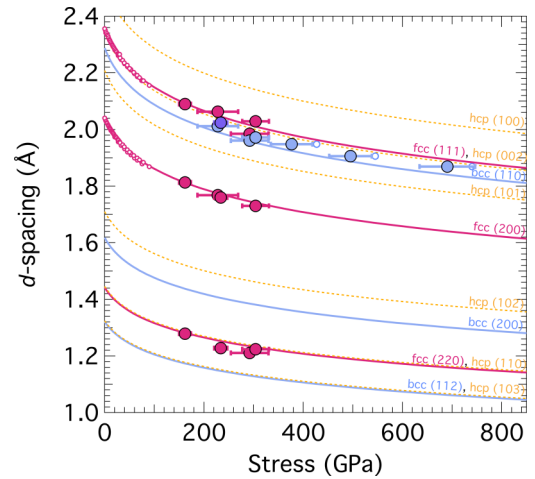

FIG. 4. Measured d spacing (filled circles) as a function of stress together with extrapolations for fcc (magenta), bcc (blue), and hcp (yellow) phases using 300-K equation-of-state (EOS) data ($K_0 = 167$, $K_0' = 5.71$; see text) [2]. The purple data point at 234 GPa represents an fcc (111)–bcc (110) doublet whose individual positions could not be constrained due to overlap with a pinhole peak (see text and the Supplemental Material [34]). Due to the higher temperatures achieved in ramp compression (see discussion in text), it is expected that the resulting d spacings will be smaller than those predicted by extrapolations of 300-K data. The hcp diffraction pattern was calculated assuming an ideal c-to-a ratio. Unfilled magenta circles show well-calibrated 300-K static data for gold [15]. Error bars that are smaller than the symbol are not shown. Unfilled blue circles represent d spacing if diamond loses strength on release as discussed in the text.

Diffraction data from the lowest-stress shot [162(12) GPa] are consistent with the fcc phase (Fig. 4). In this shot, the peak at 2.081(10) Å is indexed as the fcc (111), the peak at 1.809(14) Å is indexed as the fcc (200), and the peak at 1.277(10) is indexed as the fcc (220). The hcp phase can be ruled out on the following grounds. While the peaks at 2.081(10) and 1.277(10) Å could be assigned to the hcp (002) and (110) reflections, respectively, no other peaks indexable to the hcp polymorph were observed. Furthermore, the intensity of the (002) reflection is expected to be the weakest of the hcp (100), (002), and (101) triplet. Finally, an hcp assignment cannot provide an explanation for the peak at 1.809(14) Å. We can similarly rule out the double-hexagonal-close-packed phase and other extended stacking sequence phases predicted for gold [9,25,26]. The uncertainties of our measured d spacings preclude us from drawing any conclusions regarding the presence of stacking faults in the fcc phase.

We interpret the diffraction for shots between 228(41) and 304(27) GPa as consistent with diffraction from both fcc and bcc gold. Other ramp-compression experiments have also observed multiphase assemblages in other metals such as the fcc-hcp and bcc-hcp mixed phases observed in ramp-compressed aluminum [32]. A mixed-phase interpretation agrees with previous laser-based shock-compression experiments on gold, which reported a mixed-phase region along the shock Hugoniot [10,11]. In ramp-compression shots between 228(41) and 304(27) GPa, the peak between approximately 1.7 and 1.85 Å is assigned to the (200) peak of the fcc phase,

and the peak at ∼1.2 Å is assigned to the fcc (220) providing clear evidence for the persistence of the fcc phase at these stresses (Fig. 4). The (200) and (220) peaks are not both detectable at every stress within this range, possibly due to texturing or the strong x-ray background. For three of these shots [228(41), 292(38), and 304(27) GPa], the most intense diffraction peak, between approximately 1.9 and 2.1 Å, is broad and asymmetric (see Figs. S5 and S6 of the Supplemental Material). We interpret this feature as two closely spaced peaks with the higher *d*-spacing component of the doublet assigned to fcc (111), while the lower *d*-spacing component is assigned to bcc (110) [34]. Fitting only a single peak to this feature yields a lattice parameter inconsistent with either the fcc or bcc phases. The most intense diffraction peak for the shot at 234(13) GPa is overlain by diffraction from the ambient pinhole material (Pt in this case), complicating phase assignment for this shot. For consistency with the other data, this shot is assigned as mixed fcc-bcc, but the precise peak locations cannot be well constrained.

For the four experiments between 228 and 304 GPa where evidence for both fcc and bcc diffraction is observed, the x-ray probe time for these shots occurred after peak stress [34]. That is, the samples were initially compressed to higher stresses, typically 320–350 GPa, and then partially released to the probed stresses. It is therefore possible that the bcc phase was produced at the maximum compression and persisted on release back into the fcc stability region due to the kinetics of the phase transformation. This may provide an explanation for the broad mixed-phase region observed and would result in better agreement with the theoretically predicted phase diagram.

At stresses between 377(42) and 690(56) GPa, only one diffraction peak, lying between 1.940(12) and 1.864(12) Å, is observed (see Fig. 4). We assign this peak to the bcc (110). The presence of a single peak is consistent with the significantly higher expected intensity of bcc (110) relative to bcc (200) or (211), the next two most intense reflections for this structure. Furthermore, previous ramp-compression experiments have observed only the bcc (110) reflection in molybdenum [30], tin [31], and aluminum [32] at megabar to multimegabar pressures. In these shots, the x-ray source probed the sample at or before peak compression such that only compression states were sampled [34].

Further evidence in support of identification of the bcc polymorph is obtained by comparing the densities of possible phase assignments (Fig. 5, and Table S2 of the Supplemental Material). The 300-K static-compression data follow a cooler compression path than our ramp data and should consequently represent a density upper bound at equivalent stresses and pressures. Due to shock-induced heating, the Hugoniot should represent a lower bound to the density at a given stress. At the highest stresses (>333 GPa), where only one sample diffraction peak is observable, assignment to the (111) reflection of the fcc phase yields densities up to 1 g/cm³, or ∼3%, higher than the upper limit of 300-K extrapolations for the density of the fcc phase [34], while assignment to the bcc phase yields densities between the range of 300-K extrapolations and Hugoniot densities (Fig. 5 and the Supplemental Material [34]). Based on the *d* spacing and relative intensity of diffraction lines as well as calculated densities, the bcc structure
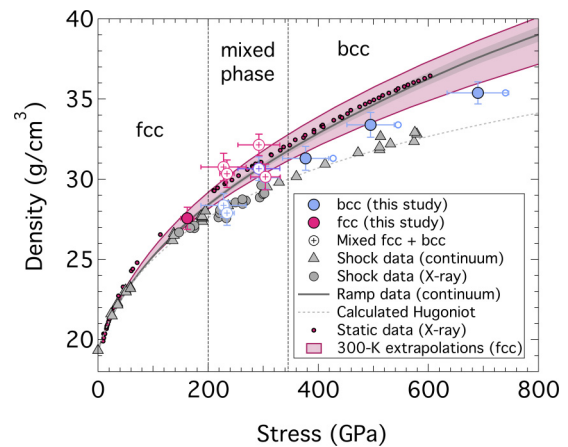

FIG. 5. Calculated density as a function of phase assignment for gold. Magenta and blue circles represent densities calculated assigning the primary diffraction peak of each shot to either fcc (111) or bcc (110) respectively, while purple represents a peak which was overlain by diffraction from the ambient pinhole material (see text). The shaded pink region represents the extrapolated range of literature 300-K isotherms [1,4], while the filled pink circles represent 300-K static-compression data [24]. The solid gray line and shaded gray area represent continuum ramp-compression data from the National Ignition Facility [49]. Shock-compression data are separated into those whose densities were measured via continuum methods (gray triangles) and those whose densities were measured via x-ray diffraction (gray circles). Data are from Refs. [1,3,4,10,11,50,51]. The calculated Hugoniot is from Ref. [6].

provides the most consistent explanation for our observed data at 377(42) GPa and above.

IV. DISCUSSION

A. Hydrodynamic approximation and strength

Gold is well known as a soft metal with low yield strength at near-ambient conditions. In general, the strength of a material under dynamic loading will depend on various factors such as compression, temperature, strain rate, and total plastic strain [52]. The dynamic strength of gold was recently reported up to 400 GPa from wave profile measurements during ramp-release experiments (∼100-ns timescale) using the Sandia Z-machine [53]. Linear extrapolation of these data (and ignoring any effects of the phase change) to the stress range of this study suggests a nonhydrostatic correction to our data of at most ∼10 GPa at 690 GPa, or about 1.5% of the total stress. At every stress sampled, the nonhydrostatic correction is within the uncertainty of the measured stress, which suggests that the hydrodynamic approximation, in which it is assumed that peak longitudinal stress σ approximates the hydrostatic pressure P, is reasonable for this material over the stress-pressure range of our study.

B. Temperature estimation

Temperature was not directly measured in these experiments. In an ideal ramp experiment in which there is no plastic work, the temperature rise is expected to be isentropic [29]. A lower bound to the temperature in our experiments
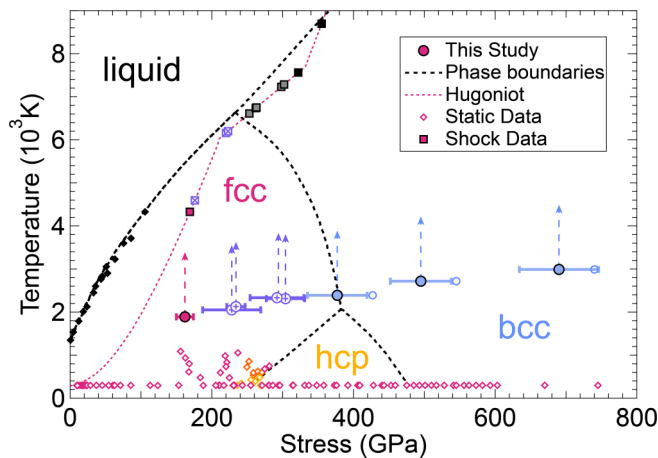
FIG. 6. The phase diagram of gold including selected experimental data and calculated phase boundaries. Symbol colors correspond to phase assignment: magenta, fcc; yellow, hcp; blue, bcc; orange, mixed fcc and hcp; purple, mixed fcc and bcc; gray, mixed bcc and melt; black, melt. Unfilled blue circles represent stress assignment if diamond loses strength on release, as discussed in the text. Ramp-compression temperatures represent a lower bound as discussed in the text. Black diamonds represent experimental determinations of the melt curve under static compression [54]. Open diamonds represent static-compression data [9,23,24]. Squares represent shock-compression data [10,11]. Reported Hugoniot temperatures are determined as described in Refs. [10,11]. The Hugoniot path is from Ref. [55]. Calculated phase boundaries are from Ref. [6].

can then be obtained by combining the Hugoniot temperature rise due to the initial shock wave transmitted through the diamond with further isentropic heating up to the final stress. The stress of the shock transmitted into gold by diamond was taken to be 79 GPa, which is the average of the initial shocks, which ranged from 60 to 94 GPa. The associated shock temperature, 1343 K, was taken from the theoretically calculated pressure-temperature relationship along the Hugoniot in Ref. [6]. Finally, the temperature achieved upon ramp compression to the final stress was calculated assuming isentropic compression:

$$T = T_H \exp\left[\frac{\gamma_0}{V_0}(V_H - V)\right], \qquad (3)$$

where γ_0 is the ambient-pressure Grüneisen parameter, T_H and V_H refer to the initial shocked state, and V_0 refers to the ambient specific volume. The Grüneisen parameter ($\gamma_0 = 2.97$ [3]) was assumed to be a function of volume only [$q = 1$ where $\gamma(V) = \gamma_0(V/V_0)^q$]. The resultant temperatures, which ranged from 2300 to 3300 K over a stress range of 162(12) to 690(56) GPa, were taken as a lower bound (Fig. 6). The melting curve serves as an extreme upper temperature limit as our data show that gold remains solid over the range of this study (Fig. 6). Over the pressure range of our data, associated melting temperatures range from ∼4000 K to more than 10 000 K with good agreement between static melting data which extend to 110 GPa [54] and theoretical calculations which extend into the terapascal regime [6]. Densities obtained in this study are close to those determined under static loading and are greater than those along the Hugoniot

by 4% at 162(12) GPa increasing to 6% at 690(56) GPa. This likely reflects temperature differences, and implies that at the highest pressures, our data are at much lower temperatures than the Hugoniot or the melting curve. This is validated by the low strength of gold, which suggests that temperatures will be closer to the principal isentrope than the Hugoniot or the melt curve, as the main entropic contribution to temperature rise is plastic work heating due to strength.

C. Comparison with previous studies

This study provides the first determination of the atomic-level structure of gold under ∼10-ns ramp compression, reaching up to nearly 700 GPa. We observe a transition from the ambient fcc structure to a bcc structure beginning at 228(41) GPa. Our results might appear to be inconsistent with most theoretical studies at 0–300 K, which predict transformation to an hcp or dhcp phase [5,7,9,25]. However, theoretical studies at elevated temperatures are more limited, and only Ref. [6] has examined the high-temperature phase diagram in detail. That study reported that the hcp phase is stable at room temperature from about 250 to 475 GPa followed by transformation to the bcc phase (see Fig. 6). The stability field of the hcp phase contracts with temperature, and the fcc phase is predicted to transform directly to the bcc phase above 2000 K, with a negative Clapeyron slope. Our results are consistent with Ref. [6] in that the minimum expected temperatures in our experiments lie above the stability field of the hcp phase. This is also consistent with the results of static experiments which reported the hcp phase at moderate temperatures [9].

Recently, ramp-compression data on gold to 1158 GPa were reported based on experiments at the National Ignition Facility (NIF) and the Z-machine [49]. While our results overlap within uncertainty at lower stresses, the Omega data reported here are less dense at the highest stress. There are several important differences between ramp compression at NIF and Omega that could contribute to this difference. First, the longer compression time (30 vs 10 ns) and lower initial shock (30–35 vs 60–94 GPa) in the NIF experiments are expected to result in a cooler compression path. Secondly, for the Omega experiments, the large impedance mismatch between gold and diamond may contribute to uncertainty in stress, as seen in similar experiments on dense metals (Fig. 7, Cu, Sn, Fe-Si). Future experiments will be needed to better understand the differences between the two techniques. Note that the NIF experiments only measured density, and no constraints on the atomic-level structure of gold were obtained in those experiments.

Our results are also consistent with recent shock wave studies that identified a phase transformation from the fcc structure to the bcc structure along the Hugoniot. Furthermore, the transformation is observed to occur through a mixed-phase region along both types of loading paths [10,11], with the onset of transformation occurring at lower pressures than theoretically predicted [6].

The appearance of the bcc phase in this study occurs at 228(41) GPa with a temperature lower bound of 2300 K. Predicted equilibrium transition pressures range from 380 GPa at 2300 K to 233 GPa at 6600 K [6]. The predicted equilibrium transition pressure is above 255 GPa at all tem-
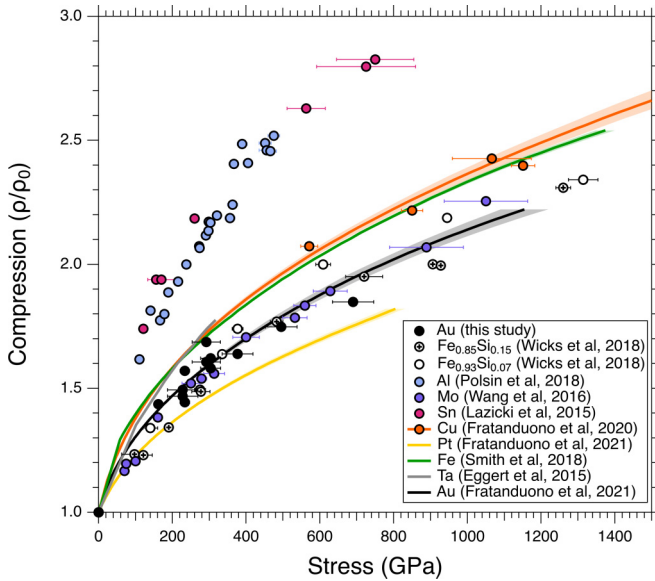
FIG. 7. Comparison of compression curves under ramp compression for metals examined to date. Solid lines represent studies for which density was measured at the continuum level, while circles represent studies for which x-ray diffraction data were used to determine density. ρ_0 is the density of the stable phase at ambient conditions. Data are from Refs. [30,31,33,46,47,49,57,58]. TBP, to be published.

peratures below 6300 K. However, as discussed above, the x-ray probe time in these experiments occurred after release from peak stresses above 320 GPa, so it is possible that the phase boundary is at higher pressure. This discrepancy is also present in recent shock wave experiments in which the appearance of the bcc phase was observed at lower pressures than predicted at Hugoniot temperatures [10,11]. This indicates that the theoretical calculations may overestimate the fcc-bcc transition pressure.

The first observation of full conversion to the bcc phase was made at 377(42) GPa, which is consistent with the predicted equilibrium phase boundary [6]. While phase transition pressures are often observed to require overdriving under dynamic compression due to kinetic effects [29], a transformation occurring at lower pressures than expected is unusual, although not unprecedented, with a recent example provided by experiments on antimony [56]. Recent work quantifying stacking faults in shock-compressed metals suggest that these stacking faults can promote phase transitions [28]. A static-compression study observed a transformation from the fcc to the hcp phase at 248 GPa and 860 K [9]. As shown in Fig. 6, our minimum calculated temperatures for ramp-compressed gold lie above the maximum temperature at which hcp gold is predicted to be stable according to the theoretical calculation [6]. This can explain the difference between our results and the high-temperature diamond anvil cell experiments [9].

D. Ramp-compressed metals

Laser-based ramp compression of solids has emerged in recent years as a novel technique allowing solid materials to be probed at conditions beyond the limits imposed by static-compression technology and shock melting along the

Hugoniot. The method also allows access to intermediate-temperature states between the end members of the principal isentrope and the Hugoniot. Ramp-compression studies have been performed using interferometry on multistepped targets to constrain stress-density states at the continuum level [47,57,58] as well as time-integrated x-ray diffraction for atomic-level structural measurements [30,31,33,46,47]. In addition to laser-based ramp compression on ∼10-ns timescales, magnetic compression techniques can ramp-compress materials on ∼100-ns timescales to pressures of hundreds of gigapascals [53]. Results to date for elemental metals and alloys are summarized in Fig. 7.

Pressures above 1 TPa have been reached in x-ray diffraction studies of laser-ramped metals [31,33] with the primary limitation on peak pressure arising from decreasing signal-to-noise ratio of diffraction data at higher pressures due to the x-ray background produced by the more energetic plasma plumes required to drive such compression. Higher pressures, above 2 TPa, have been reported in continuum measurements [59], but these do not provide atomic-level structural information. These pressures are as much as five times higher than achieved in these materials using static-compression technology. Metals examined so far span a range from highly compressible (Sn, Al) to incompressible (Pt, Mo). At pressures of ∼1 TPa, the materials achieve densities about 2—3 times greater than their ambient densities. For pure metals examined by x-ray diffraction, the bcc phases were observed at the highest pressures due either to phase transitions (Sn, Al, Au) [31,46] or persistence of the ambient structure (Mo) [30] except for copper, which remains in the fcc structure based on diffraction data to 1.15 TPa, although transformation to the bcc structure was recently reported at 180 GPa under shock loading [60].

V. CONCLUSION

Gold was ramp compressed to 690(56) GPa by means of laser ablation and probed using *in situ* x-ray diffraction. The fcc phase was observed to persist to 292(38) GPa. The bcc phase was first observed as part of a mixed fcc-bcc assemblage. Complete conversion to bcc was observed at 377(42) GPa, and this phase was observed up to the peak stress of this study. These results are consistent with theoretical calculations, which predicted a high-pressure–high-temperature bcc polymorph [6,7], as well as with recent laser-based shock experiments which also observed transformation to the bcc phase through an fcc-bcc mixed-phase region [10,11]. These results are in contrast to static-compression experiments in which the hcp phase was observed under conditions of heating [9] or the fcc phase was observed to 1.065 TPa [24]. Temperatures were not directly measured in our experiment but were constrained to be between the temperatures achieved by shock loading to ∼100 GPa followed by isentropic compression to peak pressure, resulting in temperatures between 2000 and 3500 K over the pressure range of this study, and the melting curve, which ranged between 5000 and over 10 000 K. Our temperatures are likely much closer to the lower bound, as plastic work heating in gold is expected to be minimal due to its low strength. That our measured densities are close to isothermal values and much denser than Hugoniot values provides support for this

inference. High-temperature x-ray diffraction under static, ramp, and shock compression for gold at multimegabar pressures is consistent with the theoretical prediction [6] that at these pressure conditions, gold adopts the bcc structure at high temperatures and may adopt the hcp structure at moderate temperatures.

ACKNOWLEDGMENTS

[1] J. C. Jamieson, J. N. Fritz, and M. H. Manghnani, in *High-Pressure Research in Geophysics*, edited by S. Akimoto and M. H. Manghnani (Center for Academic Publications, Tokyo, 1982), pp. 27–48.

[2] A. Dewaele, P. Loubeyre, and M. Mezouar, Phys. Rev. B **70**, 094112 (2004).

[3] M. Yokoo, N. Kawai, K. G. Nakamura, K. I. Kondo, Y. Tange, and T. Tsuchiya, Phys. Rev. B **80**, 104114 (2009).

[4] B. K. Godwal and R. Jeanloz, Phys. Rev. B **40**, 7501 (1989).

[5] J. C. Boettger, Phys. Rev. B **67**, 174107 (2003).

[6] N. A. Smirnov, J. Phys.: Condens. Matter **29**, 105402 (2017).

[7] R. Ahuja, S. Rekhi, and B. Johansson, Phys. Rev. B **63**, 212101 (2001).

[8] P. Söderlind, Phys. Rev. B **66**, 176201 (2002).

[9] L. Dubrovinsky, N. Dubrovinskaia, W. A. Crichton, A. S. Mikhaylushkin, S. I. Simak, I. A. Abrikosov, J. S. de Almeida, R. Ahuja, W. Luo, and B. Johansson, Phys. Rev. Lett. **98**, 045503 (2007).

[10] R. Briggs, F. Coppari, M. G. Gorman, R. F. Smith, S. J. Tracy, A. L. Coleman, A. Fernandez-Pañella, M. Millot, J. H. Eggert, and D. E. Fratanduono, Phys. Rev. Lett. **123**, 045701 (2019).

[11] S. M. Sharma, S. J. Turneaure, J. M. Winey, Y. Li, P. Rigg, A. Schuman, N. Sinclair, Y. Toyoda, X. Wang, N. Weir, J. Zhang, and Y. M. Gupta, Phys. Rev. Lett. **123**, 045702 (2019).

[12] D. L. Heinz and R. Jeanloz, J. Appl. Phys. (Melville, NY) **55**, 885 (1984).

[13] S. H. Shim, T. S. Duffy, and K. Takemura, Earth Planet. Sci. Lett. **203**, 729 (2002).

[14] Y. Fei, A. Ricolleau, M. Frank, K. Mibe, G. Shen, and V. B. Prakapenka, Proc. Natl. Acad. Sci. U. S. A. **104**, 9182 (2007).

[15] K. Takemura and A. Dewaele, Phys. Rev. B **78**, 104119 (2008).

[16] Y. Ye, V. B. Prakapenka, Y. Meng, and S. H. Shim, J. Geophys. Res.: Solid Earth **122**, 3450 (2017).

[17] T. Tsuchiya, J. Geophys. Res.: Solid Earth **108**, 2462 (2003).

[18] C. W. Greeff and M. J. Graf, Phys. Rev. B **69**, 054107 (2004).

[19] P. Renaudin, V. Recoules, P. Noiret, and J. Clérouin, Phys. Rev. E **73**, 056403 (2006).

[20] K. Widmann, T. Ao, M. E. Foord, D. F. Price, A. D. Ellis, P. T. Springer, and A. Ng, Phys. Rev. Lett. **92**, 125002 (2004).

[21] N. J. Hartley, N. Ozaki, T. Matsuoka, B. Albertazzi, A. Faenov, Y. Fujimoto, H. Habara, M. Harmand, Y. Inubushi, T. Katayama, M. Koenig, A. Krygier, P. Mabey, Y. Matsumaura, S. Matsuyama, E. E. McBride, K. Miyanishi, G. Morard, T. Okuchi1, T. Pikuz *et al.*, Appl. Phys. Lett. **110**, 071905 (2017).

[22] L. Dubrovinsky, N. Dubrovinskaia, V. B. Prakapenka, and A. Abakumov, Nat. Commun. **3**, 1163 (2012).

[23] N. Dubrovinskaia, L. Dubrovinsky, N. A. Solopova, A. Abakumov, S. Turner, M. Hanfland, E. Bykova, M. Bykov, C. Prescher, V. B. Prakapenka, S. Petitgirar, I. Chuvashova, B. Gasharova, Y. L. Mathis, P. Ershov, I. Snigireva, and A. Snigirev, Sci. Adv. **2**, e1600341 (2016).

[24] A. Dewaele, P. Loubeyre, F. Occelli, O. Marie, and M. Mezouar, Nat. Commun. **9**, 2913 (2018).

[25] Z. Liu, Y. Tao, X. Zhang, and L. Cai, Comput. Mater. Sci. **114**, 72 (2016).

[26] T. Ishikawa, K. Kato, M. Nomura, N. Suzuki, H. Nagara, and K. Shimizu, Phys. Rev. B **88**, 214110 (2013).

[27] S. M. Sharma, S. J. Turneaure, J. M. Winey, P. A. Rigg, N. Sinclair, X. Wang, Y. Toyoda, and Y. M. Gupta, Phys. Rev. X **10**, 011010 (2020).

[28] S. M. Sharma, S. J. Turneaure, J. M. Winey, and Y. M. Gupta, Phys. Rev. Lett. **124**, 235701 (2020).

[29] T. S. Duffy and R. F. Smith, Front. Earth Sci. **7**, 23 (2018).

[30] J. Wang, F. Coppari, R. F. Smith, J. H. Eggert, A. E. Lazicki, D. E. Fratanduono, J. R. Rygg, T. R. Boehly, G. W. Collins, and T. S. Duffy, Phys. Rev. B **94**, 104102 (2016).

[31] A. E. Lazicki, J. R. Rygg, F. Coppari, R. F. Smith, D. E. Fratanduono, R. G. Kraus, G. W. Collins, R. Briggs, D. G. Braun, D. C. Swift, and J. H. Eggert, Phys. Rev. Lett. **115**, 075502 (2015).

[32] D. N. Polsin, D. E. Fratanduono, J. R. Rygg, A. Lazicki, R. F. Smith, J. H. Eggert, M. C. Gregor, B. H. Henderson, J. A. Delettrez, R. G. Kraus, P. M. Celliers, F. Coppari, D. C. Swift, C. A. McCoy, C. T. Seagle, J.-P. Davis, S. J. Burns, G. W. Collins, and T. R. Boehly, Phys. Rev. Lett. **119**, 175702 (2017).

[33] J. K. Wicks, R. F. Smith, D. E. Fratanduono, F. Coppari, R. G. Kraus, M. G. Newman, J. R. Rygg, J. H. Eggert, and T. S. Duffy, Sci. Adv. **4**, eaao5864 (2018).

[34] See Supplemental Material at http://link.aps.org/supplemental/10.1103/PhysRevB.103.184109 for data tables, representative pulse shapes, stress histories, diffraction lineouts, and a visual guide to the dewarping process.

[35] J. R. Rygg, R. F. Smith, A. E. Lazicki, D. G. Braun, D. E. Fratanduono, R. G. Kraus, J. M. McNaney, D. C. Swift, C. E. Wehrenberg, F. Coppari, M. F. Ahmed, M. A. Barrios, K. J. M.

Blobaum, G. W. Collins, A. L. Cook, P. Di Nicola, E. G. Dzenitis, S. Gonzales, B. F. Heidl, M. Hohenberger *et al.*, Rev. Sci. Instrum. **91**, 043902 (2020).

[36] J. R. Rygg, J. H. Eggert, A. E. Lazicki, F. Coppari, J. A. Hawreliak, D. G. Hicks, R. F. Smith, C. M. Sorce, T. M. Uphaus, B. Yaakobi, and G. W. Collins, Rev. Sci. Instrum. **83**, 113904 (2012).

[37] P. M. Celliers, D. K. Bradley, G. W. Collins, and D. G. Hicks, Rev. Sci. Instrum. **75**, 4916 (2004).

[38] J. H. Kelly, L. J. Waxer, V. Bagnoud, I. A. Begishev, J. Bromage, B. E. Kruschwitz, T. J. Kessler, S. J. Loucks, D. N. Maywar, R. L. McCrory, D. D. Meyerhofer, S. F. B. Morse, J. B. Oliver, A. L. Rigatti, A. W. Schmid *et al.*, J. Phys. IV **133**, 75 (2005).

[39] T. R. Boehly, D. L. Brown, R. S. Craxton, R. L. Keck, J. P. Knauer, J. H. Kelly, T. J. Kessler, S. A. Kumpan, S. J. Loucks, S. A. Letzring, F. J. Marshall, R. L. McCrory, S. F. B. Morse, W. Seka, J. M. Sources, and C. P. Verdon, Opt. Commun. **133**, 495 (1997).

[40] F. Coppari, R. F. Smith, J. H. Eggert, J. Wang, J. R. Rygg, A. Lazicki, J. A. Hawreliak, G. W. COllins, and T. S. Duffy, Nat. Geosci. **6**, 926 (2013).

[41] D. E. Fratanduono, T. R. Boehly, P. M. Celliers, M. A. Barrios, J. H. Eggert, R. F. Smith, D. G. Hicks, G. W. Collins, and D. D. Meyerhofer, J. Appl. Phys. (Melville, NY) **110**, 073110 (2011).

[42] D. K. Bradley, J. H. Eggert, R. F. Smith, S. T. Prisbrey, D. G. Hicks, D. G. Braun, J. Biener, A. V. Hamza, R. E. Rudd, and G. W. Collins, Phys. Rev. Lett. **102**, 075503 (2009).

[43] J. Larsen and S. Lane, J. Quant. Spectrosc. Radiat. Transfer **51**, 179 (1994).

[44] J. R. Maw, in *Shock Compression of Condensed Matter - 2003: Proceedings of the Conference of the American Physical Society Topical Group on Shock Compression of Condensed Matter*, AIP Conference Proceedings Vol. 706 (American Institute of Physics, Woodbury, NY, 2004), p. 1217.

[45] F. Coppari, R. F. Smith, D. B. Thorn, J. R. Rygg, D. A. Liedahl, R. G. Kraus, A. Lazicki, M. Millot, and J. H. Eggert, Rev. Sci. Instrum. **90**, 125113 (2019).

[46] D. N. Polsin, D. E. Fratanduono, J. R. Rygg, A. Lazicki, R. F. Smith, J. H. Eggert, M. C. Gregor, B. H. Henderson, X. Gong, J. A. Delettrez, R. G. Kraus, P. M. Celliers, F. Coppari, D. C. Swift, C. A. McCoy, C. T. Seagle, J.-P. Davis, S. J. Burns, G. W. Collins, and T. R. Boehly, Phys. Plasmas **25**, 082709 (2018).

[47] D. E. Fratanduono, R. F. Smith, S. J. Ali, D. G. Braun, A. Fernandez-Pañella, S. Zhang, R. G. Kraus, F. Coppari, J. M. McNaney, M. C. Marshall, L. E. Kirch, D. C. Swift, M. Millot, J. K. Wicks, and J. H. Eggert, Phys. Rev. Lett. **124**, 015701 (2020).

[48] T. S. Duffy, G. Shen, D. L. Heinz, J. Shu, Y. Ma, H.-K. Mao, R. J. Hemley, and A. K. Singh, Phys. Rev. B **60**, 15063 (1999).

[49] D. E. Fratanduono, M. Millot, D. G. Braun, S. J. Ali, A. Fernandez-Pañella, C. T. Seagle, J.-P. Davis, J. L. Brown, Y. Akahama, R. G. Kraus, M. C. Marshall, R. F. Smith, E. F. O'Bannon III, J. M. McNaney, and J. H. Eggert, Science (2021), doi: 10.1126/science.abh0364.

[50] L. V. Al'tshuler, S. B. Kormer, A. A. Bakanova, and R. F. Trunin, Sov. Phys. JETP **11**, 3 (1960).

[51] S. P. Marsh, *LASL Shock Hugoniot Data* (University of California Press, Berkeley, 1980).

[52] D. J. Steinberg, S. G. Cochran, and M. W. Guinan, J. Appl. Phys. (Melville, NY) **51**, 1498 (1980).

[53] J. L. Brown, J.-P. Davis, and C. T. Seagle, Multi-megabar Dynamic Strength Measurements of Ta, Au, Pt, and Ir, J. Dyn. Behav. Mater. (2020), doi: 10.1007/s40870-020-00256-6.

[54] G. Weck, V. Recoules, J. A. Queyroux, F. Datchi, J. Bouchet, S. Ninet, G. Garbarino, M. Mezouar, and P. Loubeyre, Phys. Rev. B **101**, 014106 (2020).

[55] G. I. Kerley, Equations of State for Be, Ni, W, and Au, Tech. Rep. SAND2003-3784, Sandia National Laboratories (2003).

[56] A. L. Coleman, M. G. Gorman, R. Briggs, R. S. McWilliams, D. McGonegle, C. A. Bolme, A. E. Gleason, D. E. Fratanduono, R. F. Smith, E. Galtier, H. J. Lee, B. Nagler, E. Granados, G. W. Collins, J. H. Eggert, J. S. Wark, and M. I. McMahon, Phys. Rev. Lett. **122**, 255704 (2019).

[57] R. F. Smith, D. E. Fratanduono, D. G. Braun, T. S. Duffy, J. K. Wicks, P. M. Celliers, S. J. Ali, A. Fernandez-Pañella, R. G. Kraus, D. C. Swift, G. W. Collins, and J. H. Eggert, Nat. Astron. **2**, 452 (2018).

[58] J. H. Eggert, R. F. Smith, R. E. Rudd, D. E. Fratanduono, and D. G. Braun, High Pressure Res. **35**, 339 (2015).

[59] R. F. Smith, J. H. Eggert, R. Jeanloz, T. S. Duffy, D. G. Braun, J. R. Patterson, R. E. Rudd, J. Biener, A. E. Lazicki, A. V. Hamza, J. Wang, T. Braun, L. X. Benedict, P. M. Celliers, and G. W. Collins, Nature (London) **511**, 330 (2014).

[60] S. M. Sharma, S. J. Turneaure, J. M. Winey, and Y. M. Gupta, Phys. Rev. B **102**, 020103(R) (2020).